

Synthesis of Supported Planar Iron Oxide Nanoparticles and Their Chemo- and Stereoselectivity for Hydrogenation of Alkynes

María Tejada-Serrano,[†] Jose R. Cabrero-Antonino,^{†,‡} Virginia Mainar-Ruiz,[†] Miguel López-Haro,[§] Juan C. Hernández-Garrido,[§] José J. Calvino,[§] Antonio Leyva-Pérez,^{*,†,‡,§} and Avelino Corma^{*,†,§}

[†]Instituto de Tecnología Química, Universidad Politécnica de València-Consejo Superior de Investigaciones Científicas, Avda. de los Naranjos s/n, 46022, Valencia, Spain

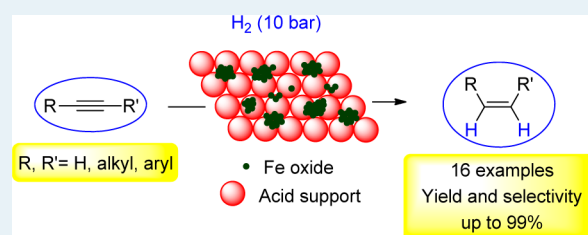
[‡]Leibniz-Institut für Katalyse e.V., Albert-Einstein-Straße 29a, 18059 Rostock, Germany

[§]Departamento de Ciencia de Materiales e Ingeniería Metalúrgica y Química Inorgánica, Universidad de Cádiz, Campus Río San Pedro, Puerto Real, 11510 Cádiz, Spain

S Supporting Information

ABSTRACT: Nature uses enzymes to dissociate and transfer H₂ by combining Fe²⁺ and H⁺ acceptor/donor catalytic active sites. Following a biomimetic approach, it is reported here that very small planar Fe^{2,3+} oxide nanoparticles (2.0 ± 0.5 nm) supported on slightly acidic inorganic oxides (nanocrystalline TiO₂, ZrO₂, ZnO) act as bifunctional catalysts to dissociate and transfer H₂ to alkynes chemo- and stereoselectively. This catalyst is synthesized by oxidative dispersion of Fe⁰ nanoparticles at the isoelectronic point of the support. The resulting Fe^{2+,3+} solid catalyzes not only, in batch, the semihydrogenation of different alkynes with good yields but also the removal of acetylene from ethylene streams with >99.9% conversion and selectivity. These efficient and robust non-noble-metal catalysts, alternative to existing industrial technologies based on Pd, constitute a step forward toward the design of fully sustainable and nontoxic selective hydrogenation solid catalysts.

KEYWORDS: iron, nanoparticles, catalysis, hydrogenation, alkynes, alkenes



1. INTRODUCTION

Metal-catalyzed alkyne semihydrogenation is a key industrial reaction to manufacture polymer-grade alkenes¹ and, in general, to synthesize new chemicals, pharmaceuticals, and some natural products with stereodefined alkene functionalities.^{2,3} Zerovalent Pd, Pt, and Ni compounds are, by far, the most used catalysts for these transformations despite the relative toxicity, low abundance, limited access, and high prices associated with these metals, particularly the Lindlar and related catalysts based on lead-poisoned Pd metal supported on inorganic oxides.^{4,5} All these drawbacks would be solved by the use of first-row early-metal catalysts, particularly metallic Fe⁰, the most earth-abundant and nontoxic early transition metal,⁶ in contrast to the less abundant and more toxic Ni. However, Fe⁰ generally catalyzes the hydrogenation of alkynes all the way to alkanes, without stopping at the intermediate alkene, even with supported⁷ or unsupported⁸ Fe⁰ NPs. In order to achieve the semihydrogenation of particular alkynes, subnanometer ligand-free,⁹ ligand-stabilized,^{10,11} or intermetallic¹² Fe⁰ catalysts must be employed.

In contrast to the aforementioned Pd, Pt, Ni, or Fe electron-rich catalysts, Nature makes use of a family of enzymes called hydrogenases,¹³ with catalytic Fe²⁺ centers and H⁺ acceptor/donor sites, to activate and transfer H₂, as is shown in Figure 1. This assisted mechanism has been successfully mimicked in the

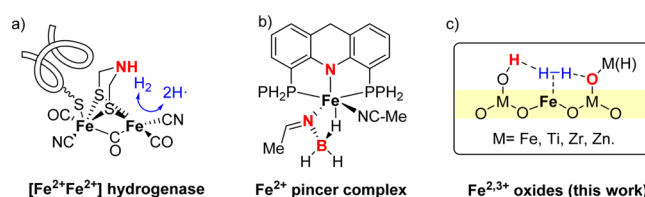


Figure 1. Structures of (a) the catalytic active site of [FeFe] hydrogenases, (b) an Fe complex that catalyzes the semihydrogenation of alkynes, and (c) inorganic oxides containing Fe^{2,3+} (this work). The assisting donor/acceptor catalytic sites are shown in red.

laboratory for the semihydrogenation of alkynes with catalytic Fe²⁺ complexes, where the ligands exert an acceptor/donor function.¹⁴ However, Fe²⁺ complexes are relatively expensive, nonrecoverable, and unsuitable for in flow applications, which severely hamper their application in industrial processes. Following this rationale, a more practical, cheap, and nontoxic biomimetic hydrogenation catalyst would consist, ideally, of a ligand-free Fe^{2,3+} compound supported on a simple solid able to exert the assisting function.¹⁵

Received: January 5, 2017

Revised: March 22, 2017

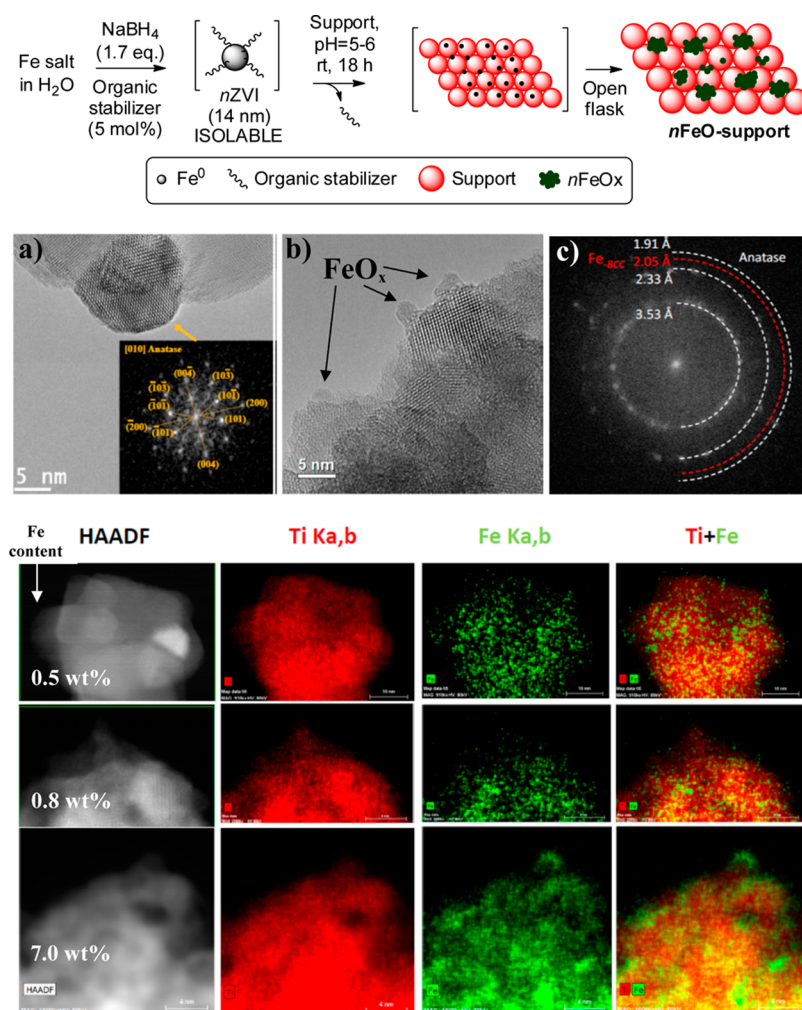


Figure 2. (top) Synthesis of $n\text{FeOx}$ -supported materials. (middle) (a) Representative bright-field high-resolution aberration-corrected transmission electron micrograph (HR-TEM) of the 0.5 and 1.0 wt % $n\text{FeOx-TiO}_2$ samples with the corresponding digital diffraction pattern (DDP) as an inset, (b) representative bright-field high-resolution aberration-corrected transmission electron micrograph (HR-TEM) of 7.0 wt % $n\text{FeOx-TiO}_2$, and (c) DDP of a medium-magnification area covering a huge number of crystallites, where the position of the diffraction rings corresponding to anatase and Fe-bcc are marked with white and red dashed lines, respectively. (bottom) Mapping of three different $n\text{FeOx-TiO}_2$ samples by X-ray energy dispersive spectroscopy (X-EDS) working in scanning transmission electron microscopy/high-angle annular dark-field mode (STEM-HAADF).

Here, it is shown that a bifunctional $\text{Fe}^{2,3+}$ solid catalyst for the semihydrogenation of alkynes can be obtained by a nonconventional synthetic method based on the redox interaction of zerovalent iron NPs ($n\text{ZVI}$)¹⁶ with inorganic oxides at the isoelectronic point. The resulting material is composed of planar monolayers of Fe oxide NPs ($n\text{FeOx}$) around 2.0 ± 0.5 nm high covering the inorganic oxide surface. The particularly small size and planar morphology of the $n\text{FeOx}$ units maximizes both the number of uncoordinated Fe cations of the NP exposed to reactants and the contact surface with the support, to give a bifunctional material able to dissociate H_2 and catalyze the chemo- and stereoselective semihydrogenation of alkynes in batch or in flow, including the semihydrogenation of acetylene in ethylene-rich streams, with >99.9% conversion and selectivity.

2. RESULTS AND DISCUSSION

2.1. Synthesis and Characterization of the Catalysts.

The incorporation of Fe^{2+} and Fe^{3+} atoms in inorganic oxides has been carried out to date by a plethora of methods including, mainly, coprecipitation,¹⁷ deposition–calcination,¹⁸ and iso-

morphic substitution.¹⁹ In all these cases, Fe tends to overlay at loadings >1 wt % or to be included within the oxide framework, which severely limits the access of reagents to potential Fe catalytic sites.²⁰ However, in the particular case of TiO_2 , three apparently unconnected issues reported in the literature coincide here to open up the possibility of a conceptually new synthesis of Fe-TiO_2 with highly accessible Fe atoms at the interphase of the support.²¹ First, the energy of formation of $\text{Fe}^0\text{—O—Ti}$ bonds is quite similar to that of $\text{Fe}^0\text{—Fe}^0$ bonds in clusters,²² in contrast to those of more oxidizing early first-row transition metals or less oxidizing late-transition-metals; thus, the smooth addition of preformed $n\text{ZVI}$ onto TiO_2 may cover the TiO_2 surface with flat layers of Fe^0 units. Second, $n\text{ZVI}$ on TiO_2 , free of stabilizing agents, rapidly reoxidizes to Fe^{2+} and Fe^{3+} oxides after air exposure, without the formation of Fe^0 cores, provided that the NPs are small enough.²³ Thus, the flat Fe^0 NPs formed on TiO_2 with $n\text{ZVI}$ should rapidly oxidize to $n\text{FeOx}$. Third, the isoelectronic points in water of $n\text{ZVI}$ (pH ~ 8) and TiO_2 (pH ~ 6) fit well in maximizing the rate of deposition of Fe atoms on the TiO_2 surface under ambient aqueous conditions.²⁴ With these three properties in hand, the

possible addition/oxidation of *n*ZVI to high-surface-area nanocrystalline TiO₂ pure anatase phase (110 m² g⁻¹, ~10 nm average size) was tested in water under open-flask conditions.

Figure 2 (top) shows that *n*ZVI of ~14 nm average size can be prepared¹⁶ from Fe salts and added as an aqueous dispersion to TiO₂ at room temperature with stirring. A complete set of conditions with different Fe salts and supports and a brief discussion on the possible role of the organic stabilizer can be found in Figure S1 in the Supporting Information, with the experimental details. Visually, it is observed that the black *n*ZVI progressively disappears from the dispersion and, at the same time, TiO₂ becomes yellowish brown. After 18 h, the solid is recovered by filtration and washed with water. Analyses by inductively coupled plasma-mass spectroscopy (ICP-MS) of the different *n*FeOx-TiO₂ materials prepared with increasing amounts of *n*ZVI show that the nominal amount of Fe employed during the synthesis is fully incorporated into the final solid, up to 5 wt % of Fe (Figure S2 and Table S1 in the Supporting Information), and then the efficiency of incorporation drops to achieve a maximum of 7 wt % of Fe. As noted in section 1, thermodynamics plays a key role in this process and, thus, a mechanism similar to that of Ostwald ripening may be operating here. Elemental analysis showed that the original carbon content in *n*ZVI (2%), corresponding to the stabilizing agent citric acid, drops to nearly 0 in the *n*FeOx-TiO₂ material. Quantitative X-ray photoelectron spectroscopy (XPS) of 7.0 wt % *n*FeOx-TiO₂, after deconvolution, shows two peaks in a 59:41 ratio with binding energies assignable to Fe³⁺/Fe²⁺ oxides, respectively, and without any trace of Fe⁰ (Figure S3 in the Supporting Information). Ti_{2p1/2} XPS measurements show that Ti⁴⁺ is the only present Ti species, without any signal of Ti³⁺ (Figure S4 in the Supporting Information),²⁵ and Brunauer–Emmett–Teller (BET) surface measurements of the material give $S_{\text{BET}} = 111.38 \text{ m}^2 \text{ g}^{-1}$ (Figure S5 in the Supporting Information), nearly identical with that of the original TiO₂ material. These results support the success of the oxidative incorporation of *n*ZVI on TiO₂ without changing the native structure of the support.

Bright-field, high-resolution aberration-corrected transmission electron micrographs (HR-TEM) of the *n*FeOx-TiO₂ materials are also shown in Figure 2. For all of these solids, TiO₂ nanocrystals assembled into large bunches of randomly oriented units can be observed, with digital diffraction patterns (DDPs) that correspond to the crystalline anatase phase (see Figure S6 in the Supporting Information for the view along the [011] axis). The fraction of rutile phase on the TiO₂ crystallites is nearly negligible (Figure S7 in the Supporting Information). Unfortunately, the presence of Fe crystalline phases for the 0.5 and 1.0 wt % Fe-TiO₂ materials was not detected with this technique, even when they were recorded at higher magnifications, since no double-diffraction Moiré-like contrasts were found.²⁶ In contrast, when the high-loaded 7.0 wt % *n*FeOx-TiO₂ catalyst was analyzed, the presence of very small FeOx NPs could clearly be observed (Figure 2 middle center; see also Figure S8 in the Supporting Information). With the hope of finding Fe on the low-loaded samples in bright-field mode, the study was expanded to a huge number of nanosized TiO₂ crystallites at medium magnifications, but only the rings of reflections of the anatase phase were found in the DDPs, without any reflection that could be assigned to Fe (Figure 2 middle right; see also Figure S9 in the Supporting

Information). These results suggest that Fe is in a very tiny, probably subnanometer form in the low-loaded samples.

The spatial distribution of Fe in all of the samples could finally be unveiled by scanning transmission electron microscopy (STEM) using both X-ray energy dispersive spectroscopy (STEM-XEDS) and high-angle annular dark-field imaging (STEM-HAADF). For that, low voltage, high current, and a sub-angstrom size electron probe were required in order to minimize electron beam damage effects while still maintaining a good signal to noise ratio and high spatial resolution. Figure 2 (bottom) compares the Fe ($K\alpha, \beta$), Ti ($K\alpha, \beta$), and composite Fe/Ti element distribution maps for three different *n*FeOx-TiO₂ samples (see Figures S10–S15 in the Supporting Information for details). Note that Fe is clearly identified in all of the maps as isolated atoms, subnanometer-sized patches, or flat nanoparticles depending on the Fe wt % of the sample, covering to a large extent the surface of the support TiO₂ crystallites. The absence of any contrasts for 3D type FeOx nanoparticles in the HR-TEM images supports a planar morphology. Further analytical results in this STEM study (Figures S16 and S17 in the Supporting Information) confirm that the presence of Fe in the maps is not due to artifacts introduced during the acquisition of the X-EDS signals, since the areas depicting low intensities in the Fe maps show a small Fe $K\alpha$ peak at 6.4 keV, which drops down to the noise level in areas where the map shows no Fe. The quantitative analysis of the samples using *z* factors,²⁷ which is crucial to quantify light elements such as O by enabling X-ray absorption correction with simultaneous computation of the composition and mass thickness, gave Fe loadings of 0.53 ± 0.02 , 0.8 ± 0.2 , and 6.98 ± 0.02 wt %, respectively, for the three solids, very close to nominal loading and, thus, providing reliability to the Fe maps.

X-ray diffraction (XRD) of *n*FeOx-TiO₂ shows peaks corresponding to the anatase phase without any peak for the rutile phase (Figure S18 in the Supporting Information), in accordance with the HR-TEM micrographs, and no FeO diffraction peaks were found even for a 7.0 wt % *n*FeOx-TiO₂ sample. Reflectance-diffuse ultraviolet–visible spectroscopy (RDUV–vis) shows the typical band for an anatase TiO₂ phase with a small band in the visible area that corresponds to *n*FeOx, without any shift that could be assigned to doping atoms (Figure S19 in the Supporting Information). These results somewhat validate the microscopic images in Figure 2 and also support that *n*FeOx-TiO₂ is composed of planar *n*FeOx supported flat on the anatase NPs, without significant 3D Fe structures or isomorphic substitution of Ti by Fe atoms, since no rutile phases are present according to the different characterization techniques.²⁸ However, it must be noted that an amorphous structure of FeO is very likely under these conditions because of the low-temperature oxidation of Fe and, thus, plays a role among the FeO species observed.

With the aim of further simplifying the synthesis of *n*FeOx-TiO₂ and in order to bypass the isolation of *n*ZVI, a one-pot procedure from Fe salts, NaBH₄, TiO₂ and the corresponding organic stabilizer was attempted. The results showed that a material nearly identical with that starting from *n*ZVI was obtained. ICP-MS measurements showed that, as occurs in the two-step procedure, Fe is fully incorporated in the material up to 5.0 wt % (Table S1 in the Supporting Information), and elemental analyses confirmed the near absence of residual boron and organic stabilizers in the solid, with a boron and carbon content <1% of that originally introduced during the synthesis (Table S2 in the Supporting Information). These

Table 1. Results for the Reaction in Scheme 1

entry	support	Fe precursor (supported Fe (wt %))	reductant/stabilizer	T (°C)/time (h)	conversion of 1a (%)	selectivity to 2a (%)
1	TiO ₂	FeCl ₂ (7.0)	NaBH ₄ /citric acid	150/4	100	93
2		FeCl ₂ (0.5)	NaBH ₄ /citric acid	150/4	100	55
3		FeSO ₄ ·7H ₂ O (0.5)	NaBH ₄ /PVP	150/4	95	91
4		FeSO ₄ ·xH ₂ O (0.5, 99.999%)	NaBH ₄ /citric acid	150/4	100	91
5		FeCl ₂ (5.0)	NaBH ₄ /citric acid	100/20	100	83
6		FeCl ₂ (1.0)	NaBH ₄ /citric acid	100/20	100	44
7		FeCl ₂ (0.5)	NaBH ₄ /citric acid	100/20	100	5
8		FeCl ₂ (0.5)	H ₂ /–	100/20	100	10
9		FeSO ₄ ·7H ₂ O (0.5)	H ₂ /–	100/20	100	54
10	ZrO ₂	FeCl ₂ (7.0)	NaBH ₄ /citric acid	150	100	70
11		FeSO ₄ ·7H ₂ O (0.5)	NaBH ₄ /citric acid	100/20	100	72
12		FeSO ₄ ·xH ₂ O (0.5, 99.999%)	NaBH ₄ /PVP	100/20	100	94
13		FeSO ₄ ·7H ₂ O (0.5)	H ₂ /–	100/20	100	43
14	ZnO	FeCl ₂ (0.5)	NaBH ₄ /citric acid	100/20	89	82
15		FeSO ₄ ·7H ₂ O (0.5)	NaBH ₄ /citric acid	100/20	68	71
16		FeSO ₄ ·7H ₂ O (0.5)	NaBH ₄ /PVP	100/20	87	97
17		FeCl ₂ (0.5)	H ₂ /–	100/20	22	80
18		FeSO ₄ ·7H ₂ O (0.5)	H ₂ /–	100/20	28	85
19	SiO ₂	FeCl ₂ (0.5)	NaBH ₄ /citric acid	100/20	<5	
20		FeSO ₄ ·7H ₂ O (0.5)	NaBH ₄ /PVP	100/20	<5	
21		FeCl ₂ (0.5)	H ₂ /–	100/20	<5	
22		FeSO ₄ ·7H ₂ O (0.5)	H ₂ /–	100/20	<5	
23	Al ₂ O ₃	FeCl ₂ (0.5)	NaBH ₄ /citric acid	100/20	<5	
24		FeSO ₄ ·7H ₂ O (0.5)	NaBH ₄ /PVP	100/20	<5	
25		FeCl ₂ (0.5)	H ₂ /–	100/20	<5	
26		FeSO ₄ ·7H ₂ O (0.5)	H ₂ /–	100/20	<5	
27	MgO	FeCl ₂ (0.5)	NaBH ₄ /citric acid	100/20	36	80
28		FeSO ₄ ·7H ₂ O (0.5)	NaBH ₄ /citric acid	100/20	<5	
29		FeCl ₂ (0.5)	H ₂ /–	100/20	<5	
30		FeSO ₄ ·7H ₂ O (0.5)	H ₂ /–	100/20	18	85
31	charcoal	FeCl ₂ (0.5)	NaBH ₄ /citric acid	100/20	<5	
32		FeSO ₄ ·7H ₂ O (0.5)	NaBH ₄ /PVP	100/20	<5	
33		FeCl ₂ (0.5)	H ₂ /–	100/20	<5	
34		FeSO ₄ ·7H ₂ O (0.5)	H ₂ /–	100/20	<5	

analyses also revealed that ~0.05 wt % of hydrogenating metals such as Pt and Rh were present in the final material, incorporated as impurities from the Fe salt. To discard any catalytic activity of the precious metals during the hydrogenation reactions, a sample of *n*FeOx-TiO₂ starting from ultrapure >99.999% FeSO₄·xH₂O was prepared, and the corresponding ICP-MS confirmed the absence of noble metals up to the detection limit of the technique (<10 parts per million (ppm)).

Once TiO₂ was successfully employed as support for the synthesis of planar *n*FeOx species, our attention turned to ZrO₂, which may also be a suitable support for Fe. The synthesis of the corresponding *n*FeOx-ZrO₂ solids was carried out, and characterization by XPS (Figure S20 in the Supporting Information),²⁹ XRD (Figure S21 in the Supporting Information), and RDUV-vis (Figure S22 in the Supporting Information) strongly supports the formation of a material similar to *n*FeOx-TiO₂, regardless of the Fe salt or organic stabilizer employed. The only difference found with TiO₂ was a slightly higher amount of Fe²⁺ (Fe³⁺:Fe²⁺ = 21:79) by XPS. A sample with ultrapure >99.999% FeSO₄·xH₂O was also prepared.

For the sake of comparison and in accordance with the literature, Fe oxide NPs of larger size supported on TiO₂ and ZrO₂ were prepared by a typical impregnation/calcination

procedure, and a representative XRD confirms the formation of the larger FeO_x NPs (Figure S23 in the Supporting Information). A loss of ~50% of surface area for TiO₂ occurs during the calcination procedure, in contrast to the synthesis of *n*FeOx-TiO₂ (compare Figures S24 and S25 in the Supporting Information). Finally, other supports such as ZnO, SiO₂, Al₂O₃, MgO, and charcoal were also submitted to the oxidative dispersion method, shown here, as well as to the classical calcination procedure (Figure S25). All of these materials, regardless of the synthetic procedure and the Fe precursors, show an Fe loading that correlates well with the nominal amount of Fe employed during the synthesis, according to ICP-MS measurements (Table S1 in the Supporting Information).

2.2. Catalytic Results for the Semihydrogenation of Different Alkynes in Batch. Table 1 and Scheme 1 show that 1-dodecyne 1a is hydrogenated under 10 bar of H₂, at 100–150 °C, when 5 mol % with respect to Fe of *n*FeOx-TiO₂ (entries

Scheme 1. Hydrogenation of 1-Dodecyne 1a with Different Fe-Solid Catalysts

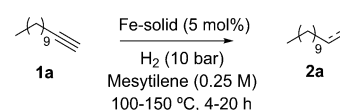
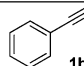
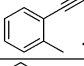
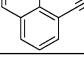
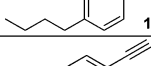
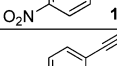
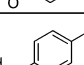
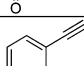
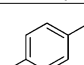
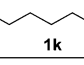
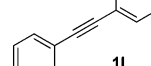
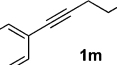
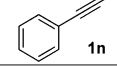
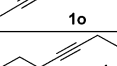

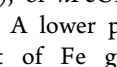


Table 2. Results for the Reaction in Scheme 2

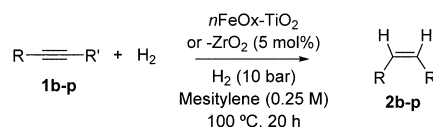
Entry	Alkyne	Support	Conversion of 1 (%)	Selectivity to 2 (%)	Conv/Select with Lindlar's catalyst (%)
1	 1b	TiO ₂	100	67	90 / 94 [Ref. 4f, 4h]
2	 1c		84	89	>95/ >95 [Ref. 4f, 4i ^a]
3	 1d		100	86	100/ 85 [Ref. 4i ^a]
4	 1e		100	68	>95/ >95 [Ref. 4f, 4h, 4i ^a]
5	 1f		80	91	-
6	 1g	ZrO ₂	100	50	100 / 97 [Ref. 4i ^a]
7	 1h		100	69	100 / 97 [Ref. 4e ^a]
8	 1i	TiO ₂	98	99	100 / 92 [Ref. 4i ^a]
9		ZrO ₂	84	99	
10	 1j	TiO ₂	72	95	100 / 92 [Ref. 4i ^a]
11		ZrO ₂	98	96	
12	 1k	TiO ₂	100	98	>99 [Ref. 4a, 4g]
13	 1l		82	91	95 / 96 [Ref. 4b, 4h]
14	 1m		78	81	92/80 [Ref. 4h]
15	 1n		100	78	92/80 [Ref. 4h]
16	 1o		100	>99	100 / 96 [Ref. 4b]
17	 1p		100	>99	100 / 96 [Ref. 4b]

^aRelated Pd-supported catalysts.

1–9), *n*FeOx-ZrO₂ (entries 10–13), or *n*FeOx-ZnO (entries 14–16) is employed as a catalyst. A lower pressure of H₂, temperature, or catalytic amount of Fe gives <50% of hydrogenation. In contrast, FeOx supported on SiO₂ (entries 19–22), Al₂O₃ (entries 23–26), MgO (entries 27–30), and charcoal (entries 31–34) give only a marginal catalytic activity even under the optimized reaction conditions. Remarkably, the hydrogenation is selective to the alkene up to 98% only when the *n*FeOx-solids are prepared by the oxidative dispersion method, including the ultrapure Fe samples (see entries 1, 3, 4, 12, and 16, in boldface). In contrast, the Fe-supported catalysts prepared by the impregnation/calcination method on the active inorganic oxides give dramatically lower catalytic activities and selectivity (entries 8, 9, 13, 17, and 18). Bare supports treated identically to the Fe-supported catalysts, with NaBH₄ or H₂ but without Fe precursors, give no catalytic activity.

Table 2 and Scheme 2 show the scope of alkynes for *n*FeOx-TiO₂ and *n*FeOx-ZrO₂ (7.0 wt %) catalysts, and the results

Scheme 2. Semihydrogenation of Alkynes **1b–p** with *n*FeOx-TiO₂ or *n*FeOx-ZrO₂ (7.0 wt %) Catalysts



show that the semihydrogenation of terminal aromatic alkynes (entries 1–11), aliphatic bis-alkynes (entry 12), and internal alkynes (entries 13–17) occurs chemo- and stereoselectively to the corresponding alkenes **2b–p** in very good yields and selectivity to the *Z* product in all cases, and other reducible functionalities such as nitro (entry 5), aldehyde (entry 7), and halide (entries 8–11) are tolerated. No further hydrogenation to the alkane product, either double bond isomerization to (*E*)-alkene or olefin migration along the alkyl chain, was detected at the end of the reaction, even after prolonged reaction times. The selectivity is, in some cases, hampered by the polymer-

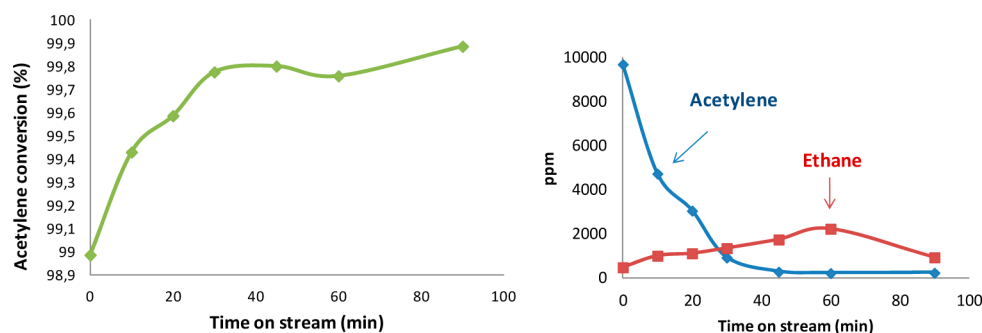


Figure 3. Removal of 1% (10000 ppm) of acetylene in a stream of ethylene by selective hydrogenation with $n\text{FeOx-TiO}_2$ catalyst (7.0 wt %): (left) acetylene conversion; (right) remaining acetylene and generated ethane. Reaction conditions: 160 °C, 4 equiv of H_2 respect to ethylene at 3 bar of pressure. The first point corresponds to 1 min reaction time.

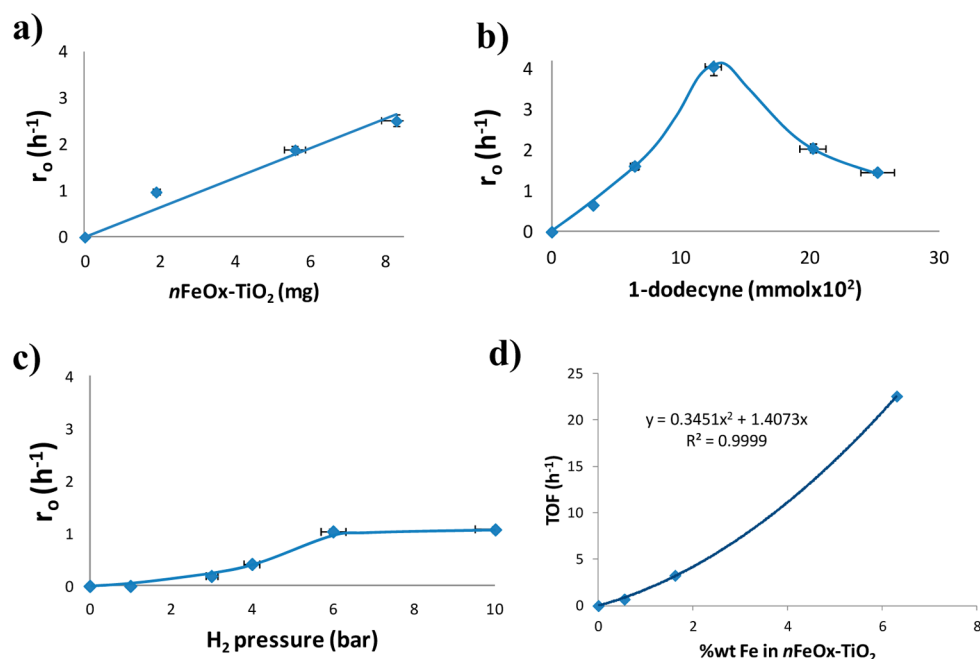


Figure 4. Initial rates for the hydrogenation of **1a** catalyzed by $n\text{FeOx-TiO}_2$ plotted vs (a) catalyst amount, (b) reagent concentration, and (c) H_2 pressure. (d) Intrinsic initial rate per surface Fe atom (turnover frequency, TOF) plotted vs Fe loading in the solid catalyst.

ization of the alkene and/or by the hydration of the alkyne to the corresponding ketone, catalyzed by the solid acid material containing some water. In addition to that, as also shown in Table 2, it must be recognized that Lindlar-type catalysts reported in the literature are much more selective and work under milder reaction conditions for these substrates.

$n\text{FeOx-TiO}_2$ was compared under the optimized reaction conditions with well-known Pd and Au hydrogenating catalysts supported on TiO_2 , and the results (Figure S26 in the Supporting Information) show that $n\text{FeOx-TiO}_2$ is significantly much more selective toward alkenes than Pd- TiO_2 or Au- TiO_2 . Note that the alkyne to alkene selectivity reported there or $n\text{FeOx}$ -supported catalysts is orthogonal and complements the chemoselective hydrogenation of nitroarenes with other Fe-supported solids.¹⁵

2.3. Catalytic Results in Flow for the Semihydrogenation of Acetylene. Raw ethylene produced by pyrolysis of hydrocarbons contains up to 1% of acetylene, and this content must be reduced to <5 parts per million (ppm) during the manufacture of polymer-grade ethylene, since higher levels of acetylene either poison or form explosive acetylides with the

metal polymerization catalysts. Currently, the semihydrogenation of ethylene is carried out with Pd supported on Al_2O_3 , modified with Ag, K, Pb, or Au additives, not only to control the hydrogenation activity of Pd but also to inhibit the potential deactivation of Pd by other molecules present in the gas stream, particularly carbon monoxide (CO).³⁰ These state of the art catalysts operate in a wide window of temperatures to resist potential runaways during the process, typically from <100 to 150 °C, and give an ethylene purity of >99.90%. Alternative catalysts based on non-noble metals supported on inorganic oxides have been developed, but they operate at >250 °C with lower catalytic efficiency, often reducing acetylene to a level of only 0.05%.³¹

The $n\text{FeOx}$ -supported catalysts developed here may catalyze the semihydrogenation of acetylene within the parameters of activity and selectivity required industrially and, potentially, circumvent CO poisoning due to the cationic nature of Fe.³² Figure 3 shows that, indeed, $n\text{FeOx-TiO}_2$ (7.0 wt % Fe) operates in flow to reduce the amount of acetylene on stream from 1% (10000 ppm) to <100 ppm with <0.2% of ethane generated. In addition, the reaction temperature can be

switched from 115 to 165 °C (Figure S27 in the Supporting Information) with a similar acetylene conversion and maintenance of the generation of ethane below 0.1%, which gives >99.9% ethylene at the reactor exit. These reaction conditions open a reasonable window of temperatures to operate the process and control the thermal runaways with the $n\text{FeOx-TiO}_2$ catalyst, while giving ethylene product with very nearly polymer grade specifications. These results constitute a step forward toward the design of efficient, robust, and versatile catalysts based on non-noble-metal catalysts that operate at temperatures <150 °C in acetylene converters.

2.4. Nature of the Fe Active Catalytic Species and Mechanism of the Semihydrogenation Reaction. Figure 4 shows the variation of the initial rate with the amount of reagents for the hydrogenation of **1a** catalyzed by $n\text{FeOx-TiO}_2$ (7.0 wt % Fe) at 150 °C, and the results show that both reagents and catalyst intervene in the rate-limiting step of the reaction. The rate variation gives a straight line with [catalyst], a volcano-type curve with [alkyne], and a sigmoidal curve with $P(\text{H}_2)$. These experimental results discard an Eley–Rideal mechanism where just one of the reactants adsorbs and reacts on the catalyst; thus, Langmuir–Hinshelwood/Hougen–Watson (LHHW) models involving the adsorption of the two reagents must be invoked. When one compares the curves in Figure 4 with the theoretical curves for the most probable LHHW models (Figure S28 in the Supporting Information), the best-fitted model to the experimental results obtained is that having one site on which the alkyne and H_2 competitively adsorb and a second site on which only the alkyne adsorbs. A possible assignation of the reaction orders for each reactant, according to the experimental curves obtained, is order 1 for the alkyne at low concentrations and -1 at high concentrations, order 1 for H_2 after an induction period and then 0 at high concentrations, and order 1 for the catalyst in all the ranges of concentrations studied. These reaction orders are in good accordance with the best-fitted LHHW model for two catalytic sites and explain the inflections in the experimental curves of the alkyne and H_2 in Figure 4: since the alkyne necessarily adsorbs more strongly than H_2 on the acid-type catalytic sites of $n\text{FeOx-TiO}_2$, H_2 adsorption becomes productive and overcomes the blockage of the active site by the alkyne only at relatively high pressures, which explains the sigmoidal curve for H_2 . Nevertheless, higher concentrations of alkyne irremediably poison the catalytic site for H_2 , which explains the volcano-type curve for the alkyne. It is known, and it was experimentally observed here under the reaction conditions in Table 1, that the Brønsted acidic M-OH sites present in $n\text{FeOx-TiO}_2$, $n\text{FeOx-ZrO}_2$, and also in the bare supports TiO_2 and ZrO_2 isomerize unsaturated C-C double bonds in the absence of H_2 , with a higher isomerization rate for the supported $n\text{FeOx}$ solids. Thus, one can assign the adsorption of alkynes to the Brønsted sites present in $n\text{FeOx-TiO}_2$ and, by elimination, the sites that competitively adsorb alkyne and H_2 must be present in $n\text{FeOx}$. These results strongly support the initial hypothesis of a cooperative mechanism between $n\text{FeOx}$ and the support.

XPS measurements of $n\text{FeOx-TiO}_2$ under H_2 at 150 °C show that the relative population of Fe^{3+} with respect to Fe^{2+} oxide stays invariable (58:42) with respect to the as-synthesized material (59:41, Figure S29 in the Supporting Information). It is also observed that the $n\text{FeOx-TiO}_2$ solids exposed to ambient conditions for prolonged times need a brief preactivation, at 150 °C under an H_2 atmosphere or at 200 °C under vacuum, to become catalytically active. In addition, induction times were

generally observed during the hydrogenation reactions. These results indicate that typical adsorbates on $n\text{FeOx}$ such as water or air poisons the catalysts, and although the results do not clarify which oxidation state for iron, Fe^{2+} , Fe^{3+} , or both, is responsible for adsorbing and reacting with H_2 , the involvement of any $\text{Fe}(0)$ species must be clearly discarded, in accordance with most of the metal complexes and natural systems studied so far.^{13,14}

Figure 4 also shows (bottom right) that the experimental data obtained for the intrinsic catalytic activity per Fe atom of different $n\text{FeOx-TiO}_2$ materials, expressed as turnover frequency (TOF), perfectly fits to a second-order polynomial curve, which is precisely the type of curve that best fits and describes the nucleation and agglomeration of isolated atoms into small NPs according to Smoluchowsky models,³³ not only theoretically for a plethora of reported systems but also experimentally for $n\text{FeOx-TiO}_2$ according to Figure 2. These results strongly suggest that neither isolated $\text{Fe}^{2,3+}$ atoms nor subnanometer FeOx clusters but rather $n\text{FeOx}$ is the catalytically active Fe species for the semihydrogenation reaction. A series of additional experiments confirm this hypothesis. First, TiO_2 and ZrO_2 impregnated with Fe^{2+} and Fe^{3+} salts, without any reduction treatment, did not give any catalytic activity under the reaction conditions in Table 1. Second, the trinuclear Fe oxide cluster $[\text{Fe}_3(\mu_3\text{-O})(\text{OAc})_6(\text{H}_2\text{O})_3]\text{OAc}$ (Figure S30 in the Supporting Information) was prepared³⁴ and tested as a catalyst for the semihydrogenation of 1-dodecyne, and no catalytic activity was found under typical reaction conditions, despite the brown Fe complex remaining intact during the reaction. Third, kinetic experiments with different $n\text{FeOx-TiO}_2$ solids showed that the alkene selectivity increases with the Fe loading, regardless of the conversion (entries 5–7 in Table 1 and Figure S31 in the Supporting Information). Fourth, commercial FeOx NPs of ~25 nm average size show some catalytic activity under optimized reaction conditions. These results discard supported isolated Fe atoms and subnanometer FeO_x species as the catalytically active species for the hydrogenation reaction, and confirm that nanometer-sized $n\text{FeO}_x$ species are responsible for H_2 (and also alkyne) adsorption and reaction during the process.

When the hydrogenation of **1a** with $n\text{FeOx-TiO}_2$ catalyst was performed under D_2 (5 bar), a kinetic isotopic effect $k_{\text{H/D}}$ (KIE) of 5.7 was obtained. This result is dramatically different from the typical KIE values for homolytic cleavage of the H-H bond (<2) and is in good agreement with a heterolytic cleavage.³⁵ In addition, the obtained deuterated product **2a** contained a significant amount (>3%) of non-deuterated H atoms, which must come from the support. These results clearly indicate that the hydroxyl groups in the support play a key role during the catalysis, and Figure 5 shows a plausible mechanism for the cis-selective semihydrogenation of alkynes catalyzed by supported $n\text{FeOx}$ on acid inorganic oxides.

The mechanism starts with the adsorption of the alkyne and H_2 in the Brønsted acid site and the $n\text{FeOx}$ catalytic sites, respectively. Note that the alkyne can also adsorb and compete with H_2 for the $\text{Fe}^{2+,3+}$ sites of $n\text{FeOx}$. Then, the hydroxyl-assisted, heterolytic H_2 dissociation occurs, leaving a hydride atom that hydrogenates the triple bond adsorbed on a Brønsted acid site. Finally, desorption of the alkene leaves a basic oxygen atom that regenerates at the expense of the protonated hydroxyl group left behind by dissociated H_2 , to regenerate the catalyst. This mechanism nicely explains the active role of

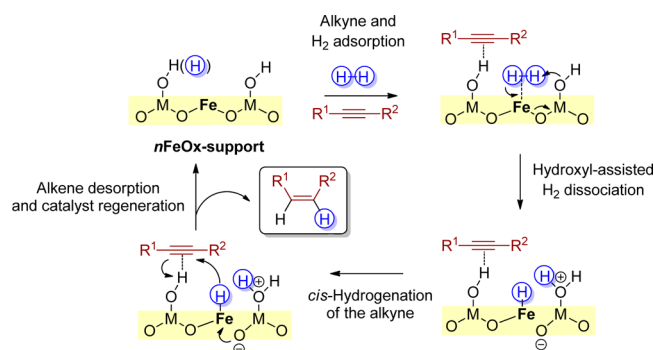


Figure 5. Plausible reaction mechanism for the cis-selective semihydrogenation of alkynes with $n\text{FeOx}$ -supported catalysts.

acid supports but it does not give a clear reason that SiO_2 and Al_2O_3 , which have less acidity but are still potentially active hydroxyl groups, lack any catalytic activity. The three active inorganic oxides, TiO_2 , ZrO_2 , and ZnO , have in common that their metallic elements are much less electronegative than Fe (1.3–1.6 vs 1.8) while, in contrast, Si and Al atoms have values similar to or higher than that of Fe (1.6–1.9). Thus, a possible explanation for the lack of activity of FeO_x on SiO_2 and Al_2O_3 is that the former, by inductive effect, increases the acidity of the hydroxyl groups only in the active inorganic oxides. This also explains the higher isomerization rate of alkenes found for $n\text{FeOx-TiO}_2$ and $n\text{FeOx-ZrO}_2$ with respect to the bare supports. The same inductive effect would decrease the per se low acidity of the hydroxyl groups in SiO_2 and Al_2O_3 , thus hampering the acid-assisted hydrogenation.

3. CONCLUSIONS

Probably planar FeOx NPs with high coverage of the surface of different acid inorganic oxides are easily formed by a one-pot redox process at room temperature. These mixed $\text{Fe}^{2+,3+}$ oxides are able to dissociate and transfer H_2 to alkynes in a chemo- and stereoselective way with the assistance of the hydroxyl groups of the inorganic oxide support. The bifunctional solid catalysts operate in batch and in flow for the cis-selective semihydrogenation of different alkynes, including acetylene, in high yields and selectivity. These results open new ways for the design of very cheap, nontoxic, ligand-free, and ambient-conditions-stable Fe solid catalysts.

4. EXPERIMENTAL SECTION

4.1. Synthesis of the Catalysts. **4.1.1. Synthesis of Zerovalent Fe NPs ($n\text{ZVI}$).** In a 50 mL flask, 231.6 mg of FeCl_2 was dissolved in 15 mL of distilled water. Then, 50 mg of citric acid was added, and 120 mg of NaBH_4 was slowly added with continuous stirring. During the addition, generation of gases was observed and a black solid was formed. The suspension was stirred until the generation of gases stopped. The solvent was decanted. The solid was washed several times with distilled water and dried under vacuum.

4.1.2. General Procedure for the Synthesis of $n\text{FeOx-MO}_2$ using $n\text{ZVI}$. In a 500 mL flask were placed 0.5 g of support and 12.5 mL of distilled water. Then, 50 mg of $n\text{ZVI}$ was added with continuous stirring. The mixture was stirred for 18 h at room temperature. Then, the solid was filtered under vacuum, washed several times with distilled water, and dried for at least 2 h under vacuum.

4.1.3. General Procedure for the One-Pot Synthesis of $n\text{FeOx-MO}_2$ Using NaBH_4 as a Reducing Agent. In a 100 mL flask were placed 2 g of support, 25 mL of an aqueous solution of iron precursor, and the stabilizing agent (0.150 equiv of citric acid or 0.007 equiv of PVP). Then, NaBH_4 was slowly added with continuous stirring. During the addition, the solution turned gray and generation of gases was observed. The mixture was stirred for 18 h at room temperature. Then, the solid was filtered under vacuum, washed several times with water, and dried for at least 2 h under vacuum. Table S3 in the Supporting Information summarizes the respective amounts for each Fe catalyst loading.

4.1.4. General Procedure for the Synthesis of $n\text{FeOx-MO}_2$ Using H_2 as a Reducing Agent. In a 100 mL flask were placed 2 g of support and 30 mL of aqueous solution of iron precursor. The mixture was stirred for 12 h in order to have a good Fe dispersion on the support. Then, the solvent was removed under vacuum and the solid obtained was dried at 80°C . When the solid was totally dried, it was treated under a nitrogen flow at 550°C over 3.5 h and activated with an air flow at 450°C (5 h) and nitrogen flow (5 h) at the same temperature. Finally, the solid was reduced under a hydrogen flow of 100 mL/min at 400°C over 3 h. Table S4 in the Supporting Information summarizes the respective amounts for each Fe catalyst loading.

4.2. Reaction Procedures (Batch and Flow). **4.2.1. General Reaction Procedure for Hydrogenation of Alkynes in Batch.** In a double-walled 2 or 6 mL vial equipped with a magnetic stirrer were placed the corresponding amount of $n\text{FeOx-metal oxide}$ catalyst and mesitylene (1 mL). Then, 0.125 mmol of alkyne was added, and the reactor was closed with a screw cap connected to a manometer. The reactor was purged three times with H_2 and finally charged with 10 bar of H_2 . The reaction mixture was placed in a preheated oil bath at $100\text{--}150^\circ\text{C}$ and magnetically stirred over 4–20 h. For kinetics, 50 μL aliquots were periodically taken and analyzed by GC using a n -alkane as an external standard. At the end of the reaction, the mixture was cooled, the solid catalyst was filtered off, and the filtrates were analyzed by GC, GC-MS, and NMR spectroscopy.

4.2.2. General Reaction Procedure for Hydrogenation of Acetylene in Flow. In a fixed-bed continuous reactor (0.5 cm diameter and 22 cm length), 50 mg of $n\text{FeOx-TiO}_2$ (7.0 wt %) was preactivated, with passing of a nitrogen flow at 200°C over 30 min. After this time, the temperature was lowered to 160°C . At this temperature, a 0.1/0.4/10 bar mixture of acetylene, hydrogen, and ethylene, respectively, was passed at 1 mL min^{-1} through the reactor, and the reaction outcome was followed with a gas chromatograph coupled on line to the reactor.

■ ASSOCIATED CONTENT

Supporting Information

The Supporting Information is available free of charge on the ACS Publications website at DOI: 10.1021/acscatal.7b00037.

General experimental section and additional figures and tables as described in the text (PDF)

■ AUTHOR INFORMATION

Corresponding Authors

*E-mail for A.L.-P.: anleyva@itq.upv.es.

*E-mail for A.C.: acorma@itq.upv.es.

ORCID

Antonio Leyva-Pérez: 0000-0003-1063-5811

Avelino Corma: 0000-0002-2232-3527

Notes

The authors declare no competing financial interest.

ACKNOWLEDGMENTS

M.T.-S. thanks the ITQ for a contract. Financial support by the “Severo Ochoa” program, the RETOS program (CTQ2014-55178-R), and the Ramón y Cajal Program (A.L.-P.) by MINECO (Spain) and also by the “Convocatoria 2014 de Ayudas Fundación BBVA a Investigadores y Creadores Culturales” is acknowledged.

REFERENCES

- (1) Trotus, I.-T.; Zimmermann, T.; Schüth, F. *Chem. Rev.* **2014**, *114*, 1761–1782.
- (2) Rosen, B. I. (UOP Inc.) U.S. Patent US4424163, 1984.
- (3) Vile, G.; Albani, D.; Almora-Barrios, N.; Lopez, N.; Perez-Ramirez, J. *ChemCatChem* **2016**, *8*, 21–33.
- (4) For Pd catalysts see: (a) McEwen, A. B.; Guttieri, M. J.; Maier, W. F.; Laine, R. M.; Shvo, Y. *J. Org. Chem.* **1983**, *48*, 4436–4438. (b) Chandrasekhar, S.; Narsihmulu, Ch.; Chandrashekar, G.; Shyamsunder, T. *Tetrahedron Lett.* **2004**, *45*, 2421–2423. (c) Domínguez-Domínguez, S.; Berenguer-Murcia, Á.; Cazorla-Amorós, D.; Linares-Solano, Á. *J. Catal.* **2006**, *243*, 74–81. (d) Conley, M. P.; Drost, R. M.; Baffert, M.; Gajan, D.; Elsevier, C.; Franks, W. T.; Oschkinat, H.; Veyre, L.; Zagdoun, A.; Rossini, A.; Lelli, M.; Lesage, A.; Casano, G.; Ouari, O.; Tordo, P.; Emsley, L.; Copéret, C.; Thieuleux, C. *Chem. - Eur. J.* **2013**, *19*, 12234–12238. (e) Mitsudome, T.; Takahashi, Y.; Ichikawa, S.; Mizugaki, T.; Jitsukawa, K.; Kaneda, K. *Angew. Chem., Int. Ed.* **2013**, *52*, 1481–1485. (f) Chan, C. W. A.; Mahadi, A. H.; Li, M. M. – J.; Corbos, E. C.; Tang, C.; Jones, G.; Kuo, W. C. H.; Cookson, J.; Brown, C. M.; Bishop, P. T.; Tsang, S. C. E. *Nat. Commun.* **2014**, *5*, 5787. (g) Vile, G.; Almora-Barrios, N.; Mitchell, S.; Lopez, N.; Perez-Ramirez, J. *Chem. - Eur. J.* **2014**, *20*, 5926–5937. (h) Markov, P. V.; Bragina, G. O.; Baeva, G. N.; Mashkovskii, I. S.; Rassolov, A. V.; Yakushev, I. A.; Vargaftik, M. N.; Stakheev, A. Y. *Kinet. Catal.* **2016**, *57*, 625–631. (i) Jagtap, S. A.; Sasaki, T.; Bhanage, B. M. *J. Mol. Catal. A: Chem.* **2016**, *414*, 78–86.
- (5) For Ni catalysts see: (a) Studt, F.; Abild-Pedersen, F.; Bligaard, T.; Sørensen, R. Z.; Christensen, C. H.; Nørskov, J. K. *Science* **2008**, *320*, 1320–1322. (b) Carenco, S.; Leyva-Pérez, A.; Concepción, P.; Boissière, C.; Mézailles, N.; Sanchez, C.; Corma, A. *Nano Today* **2012**, *7*, 21–28.
- (6) (a) Bauer, I.; Knölker, H.-J. *Chem. Rev.* **2015**, *115*, 3170–3387. (b) Fürstner, A. *ACS Cent. Sci.* **2016**, *2*, 778–789.
- (7) (a) Stein, M.; Wieland, J.; Tölle, P. S. F.; Mülhaupt, R.; Breit, B. *Adv. Synth. Catal.* **2011**, *353*, 523–527. (b) Hudson, R.; Hamasaka, G.; Osako, T.; Yamada, Y. M. A.; Li, C.-J.; Uozumi, Y.; Moores, A. *Green Chem.* **2013**, *15*, 2141–2148.
- (8) (a) Phua, P.-H.; Lefort, L.; Boogers, J. A. F.; Tristany, M.; de Vries, J. G. *Chem. Commun.* **2009**, 3747–3749. (b) Rangheard, C.; de Julián Fernández, C.; Phua, P.-H.; Hoorn, J.; Lefort, L.; de Vries, J. G. *Dalton Trans.* **2010**, *39*, 8464–8471. (c) Hudson, R.; Rivière, A.; Cirtiu, C. M.; Luska, K. L.; Moores, A. *Chem. Commun.* **2012**, *48*, 3360–3362. (d) Kelsen, V.; Wendt, B.; Werkmeister, S.; Junge, K.; Beller, M.; Chaudret, B. *Chem. Commun.* **2013**, *49*, 3416–3418.
- (9) (a) Gieshoff, T. N.; Villa, M.; Welther, A.; Plois, M.; Chakraborty, U.; Wolf, R.; von Wangelin, A. J. *Green Chem.* **2015**, *17*, 1408–1413. (b) Gaertner, D.; Welther, A.; Rad, B. R.; Wolf, R.; von Wangelin, A. J. *Angew. Chem., Int. Ed.* **2014**, *53*, 3722–3726.
- (10) Gieshoff, T. N.; Welther, A.; Kessler, M. T.; Precht, M. H. G.; von Wangelin, A. J. *Chem. Commun.* **2014**, *50*, 2261–2264.
- (11) Pittman, C. U., Jr.; Ryan, R. C.; McGee, J. J. *Organomet. Chem.* **1979**, *178*, C43–C49.
- (12) (a) Thompson, A. F., Jr.; Wyatt, S. B. *J. Am. Chem. Soc.* **1940**, *62*, 2555–2556. (b) Thompson, A. F., Jr.; Shaw, E. N. *J. Am. Chem. Soc.* **1942**, *64*, 363–366. (c) Armbrüster, M.; Kovnir, K.; Friedrich, M.; Teschner, D.; Wowsnick, G.; Hahne, M.; Gille, P.; Szentmiklósi, L.; Feuerbacher, M.; Heggen, M.; Girgsdies, F.; Rosenthal, D.; Schlögl, R.; Grin, Y. *Nat. Mater.* **2012**, *11*, 690–693.
- (13) (a) Lubitz, W.; Ogata, H.; Rüdiger, O.; Reijerse, E. *Chem. Rev.* **2014**, *114*, 4081–4148. (b) Brazzolotto, D.; Gennari, M.; Queyriaux, N.; Simmons, T. R.; Pécaut, J.; Demeshko, S.; Meyer, F.; Orío, M.; Artero, V.; Duboc, C. *Nat. Chem.* **2016**, *8*, 1054–1060. (c) Ford, C. L.; Park, Y. J.; Matson, E. M.; Gordon, Z.; Fout, A. R. *Science* **2016**, *354*, 741–743.
- (14) (a) Bianchini, C.; Meli, A.; Peruzzini, M.; Frediani, P.; Bohanna, C.; Esteruelas, M. A.; Oro, L. A. *Organometallics* **1992**, *11*, 138–145. (b) Srimani, D.; Diskin-Posner, Y.; Ben-David, Y.; Milstein, D. *Angew. Chem., Int. Ed.* **2013**, *52*, 14131–14134. (c) Zell, T.; Milstein, D. *Acc. Chem. Res.* **2015**, *48*, 1979–1994.
- (15) Jagadeesh, R. V.; Surkus, A.-E.; Junge, H.; Pohl, M.-M.; Radnik, J.; Rabeah, J.; Huan, H.; Schünemann, V.; Brückner, A.; Beller, M. *Science* **2013**, *342*, 1073–1076.
- (16) Stefaniuk, M.; Oleszczuk, P.; Ok, Y. S. *Chem. Eng. J.* **2016**, *287*, 618–632.
- (17) García-Aguilar, J.; Miguel-García, I.; Juan-Juan, J.; Such-Basáñez, I.; San Fabián, E.; Cazorla-Amorós, D.; Berenguer-Murcia, Á. *J. Catal.* **2016**, *338*, 154–167.
- (18) Spetz, R.; Marchetti, S. G.; Ulla, M. A.; Lombardo, E. A. *J. Catal.* **2000**, *194*, 167–174.
- (19) Carrettin, S.; Hao, Y.; Aguilar-Guerrero, V.; Gates, B. C.; Trasobares, S.; Calvino, J. J.; Corma, A. *Chem. - Eur. J.* **2007**, *13*, 7771–7779.
- (20) (a) Tauster, S. J. *Acc. Chem. Res.* **1987**, *20*, 389–394. (b) Corma, A.; Serna, P.; Concepción, P.; Calvino, J. J. *J. Am. Chem. Soc.* **2008**, *130*, 8748–8753.
- (21) Ge, H.; Zhang, B.; Gu, X.; Liang, H.; Yang, H.; Gao, Z.; Wang, J.; Qin, Y. *Angew. Chem., Int. Ed.* **2016**, *55*, 7081–7085.
- (22) Grüneboh, A.; Entel, P.; Herper, H. C. *Phys. Rev. B: Condens. Matter Mater. Phys.* **2013**, *88*, 155401.
- (23) Berry, F. J.; Jobson, S.; Liwu, L.; Strange, R.; Changhai, X. *Hyperfine Interact.* **1990**, *57*, 1753–1758.
- (24) Ji, Y. *Colloids Surf., A* **2014**, *444*, 1–8.
- (25) Larichev, Y. V.; Netskina, O. V.; Komova, O. V.; Simagina, V. I. *Int. J. Hydrogen Energy* **2010**, *35*, 6501–6507.
- (26) (a) Bernal, S.; Botana, F. J.; Calvino, J. J.; Cifredo, G. A.; Pérez Omil, J. A.; Pintado, J. M. *Catal. Today* **1995**, *23*, 219–250. (b) López-Haro, M.; Delgado, J. J.; Hernández-Garrido, J. C.; López-Castro, J.; Mira, C.; Trasobares, S.; Hungria, A. B.; Pérez-Omil, J. A.; Calvino, J. J. Nanoparticles. In *Handbook of Nanoscience*; Van Tendeloo, G., Van Dyck, D., Pennycuik, S. J., Eds.; Wiley-VCH: Weinheim, Germany, 2012; Vol. 2, pp 879–960.
- (27) Watanabe, M.; Williams, D. B. *J. Microsc.* **2006**, *221*, 89–109.
- (28) Rui, Z.; Chen, L.; Chen, H.; Ji, H. *Ind. Eng. Chem. Res.* **2014**, *53*, 15879–15888.
- (29) Bespalov, I.; Datler, M.; Buhr, S.; Drachsel, W.; Rupprechter, G.; Suchorski, Y. *Ultramicroscopy* **2015**, *159*, 147–151.
- (30) Bos, A. N. R.; Westerterp, K. R. *Chem. Eng. Process.* **1993**, *32*, 1–7.
- (31) Brophy, J. H.; Nock, A. (The British Petroleum Company) U.S. Patent US4705906, 1987.
- (32) Cabrero-Antonino, J. R.; Tejada-Serrano, M.; Quesada, M.; Vidal-Moya, J. A.; Leyva-Pérez, A.; Corma, A. *Chem. Sci.* **2017**, *8*, 689–696.
- (33) Kiss, L. B.; Söderlund, J.; Niklasson, G. A.; Granqvist, C. G. *Nanotechnology* **1999**, *10*, 25–28.
- (34) Matsuo, T.; Murata, N.; Mori, H. (Mitsubishi Rayon Co.) Eur. Patent EP2889284A1, 2015.
- (35) Liu, P.; Zhao, Y.; Qin, R.; Mo, S.; Chen, G.; Gu, L.; Chevrier, D. M.; Zhang, P.; Guo, Q.; Zang, D.; Wu, B.; Fu, G.; Zheng, N. *Science* **2016**, *352*, 797–800.